Supplementary Information (SI) for EES Solar.

Supplementary Information

Tuning the surface nanoroughness of the recombination junction for high-performance perovskite-silicon tandem solar cells

Yifeng Zhao[1*], Esma Ugur[2,3*], Arsalan Razzaq[2], Thomas G. Allen[2], Paul Procel[1], Adi Prasetio[2], Imil F. Imran[2], Cem Yilmaz[3], Rik Hooijer[3], Jian Huang[3], Katarina Kovačević[1], Yi Zheng[1], Luana Mazzarella[1], Erkan Aydin[3], Stefaan De Wolf[2], Olindo Isabella[1]

[1] Photovoltaic Materials and Devices, Delft University of Technology, 2628 CD, Delft, The Netherlands

[2] Center for Renewable Energy and Storage Technologies (CREST), Physical Sciences and Engineering Division (PSE), King Abdullah University of Science and Technology (KAUST), Thuwal 23955-6900, Saudi Arabia

[3] Department of Chemistry, Ludwig-Maximilians-Universität München (LMU), 81377, Munich, Germany

[*] Both authors have contributed equally.

Corresponding authors:

Erkan Aydin (erkan.aydin@cup.uni-muenchen.de), Stefaan De Wolf (stefaan.dewolf@kaust.edu.sa), Olindo Isabella (O.Isabella@tudelft.nl)

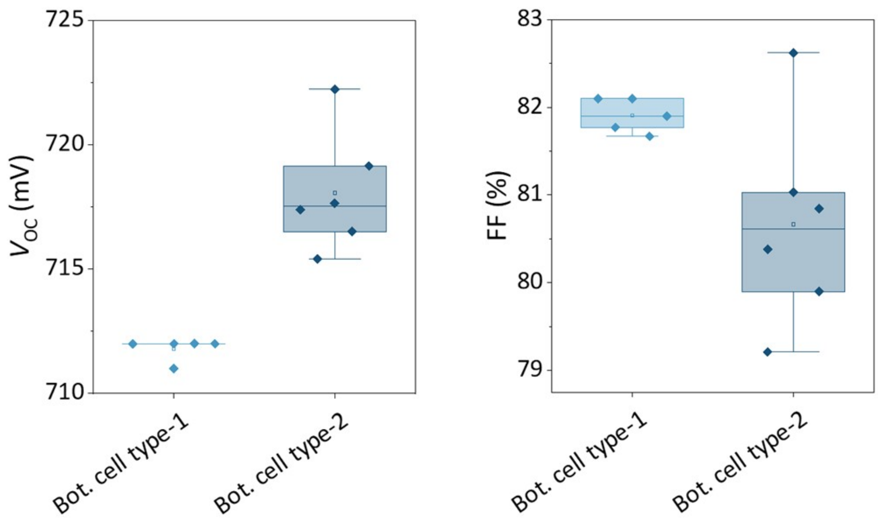

Figure S1. The V_{OC} and FF for the single-junction SHJ solar cells used in tandem solar cells shown in Figure 1. The spread of the parameters originates from process-related variability, mainly due to minor non-uniformities during thin-film depositions.

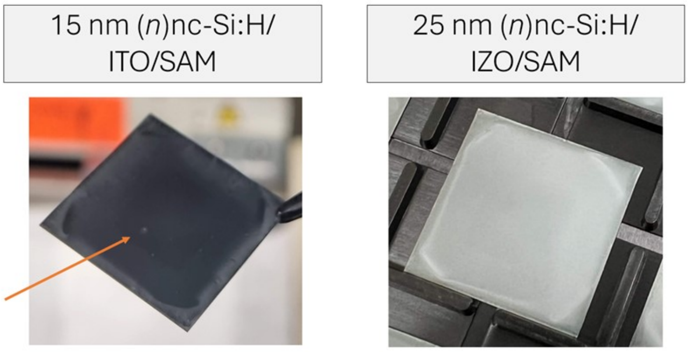

Figure S2. Photographs of perovskite thin films deposited on silicon bottom cells based on 15-nm-thick and 25-nm-thick (*n*)nc-Si:H layers. There are pinhole formation and film defects on the sample based on 15-nm-thick (*n*)nc-Si:H layer.

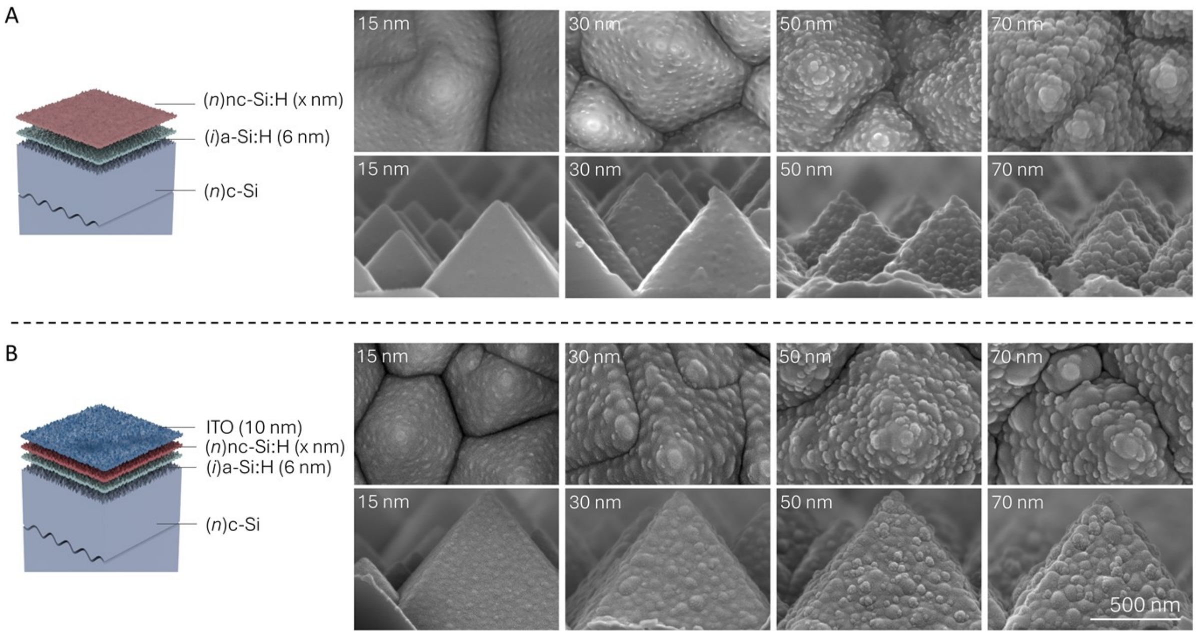

Figure S3. The schematics and SEM micrographs (with top and bottom rows displaying top views and cross-sectional views, respectively) of (*i*)a-Si:H-coated (6-nm-thick) textured c-Si samples with varied thicknesses of (*n*)nc-Si:H layers **A** without and **B** with 10 nm ITO layers. The thicknesses indicated in the figures are estimated based on the measured deposition rate on co-deposited flat samples. The addition of a 10-nm-thick ITO layer on top of the (*n*)nc-Si:H layers resulted in a more apparent surface nanoroughness across all samples. The thin ITO layer resulted in densely packed, fine-grained nanostructures presumably related to its crystalline structure.[1,2]

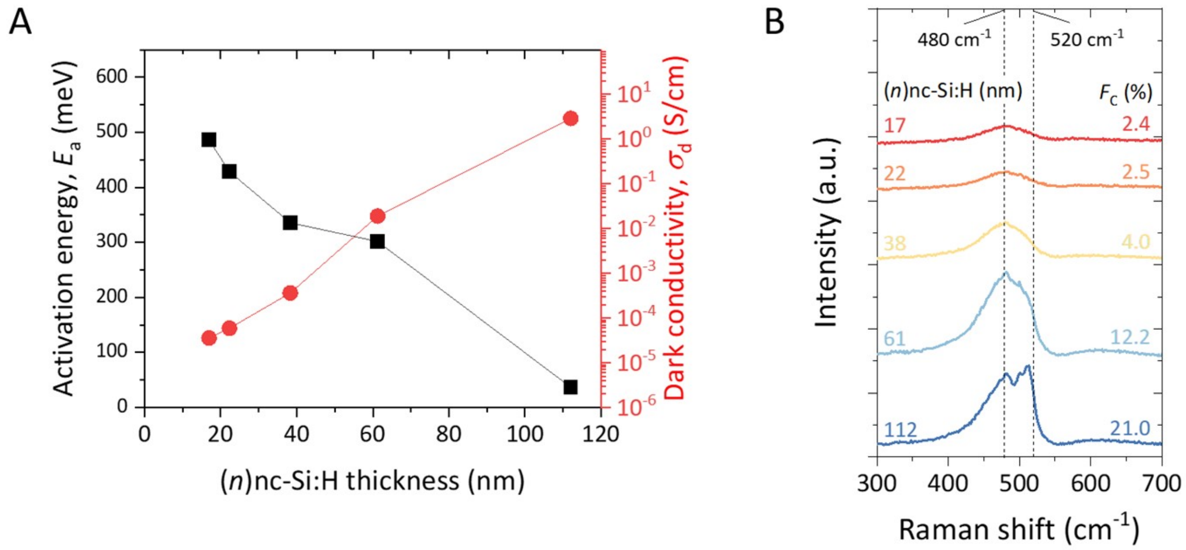

Figure S4. **A** The activation energy (E_a), dark conductivity (σ_d) and **B** Raman spectra and crystalline fraction (F_C) of (*n*)nc-Si:H layers with varied thicknesses deposited on (*i*)a-Si:H-coated (10-nm-thick) glass substrates. Note, as the green laser (λ_{laser} = 514 nm) has a penetration depth of a few hundred nanometers in the studied (*n*)nc-Si:H layers, their crystalline fraction is underestimated due to non-negligible signals from the 10-nm-thick (*i*)a-Si:H layer underneath.

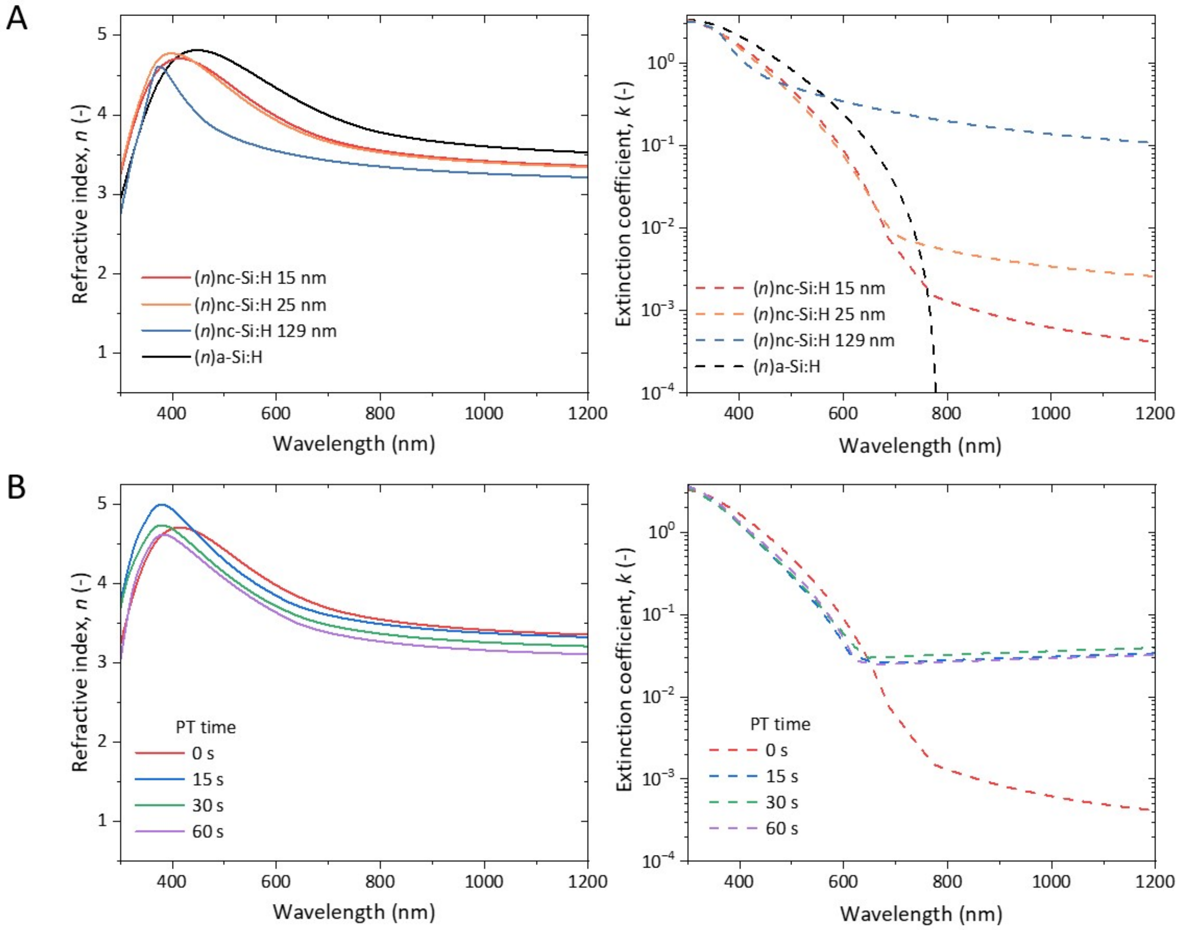

Figure S5. The optical constants of (*n*)nc-Si:H layers with **A** varied thicknesses and **B** 15-nm-thick layers with different PT durations. In **A**, the optical constants of 6-nm-thick (*n*)a-Si:H are added for comparisons. All samples feature 10-nm-thick (*i*)a-Si:H layers underneath the (*n*)nc-Si:H layers to extract device-relevant layer properties. The (*n*)nc-Si:H layers show lower absorption at shorter wavelengths and higher absorption at longer wavelengths compared with the (*n*)a-Si:H layer. This behavior arises from the coexistence of amorphous and nanocrystalline phases in (*n*)nc-Si:H layers, which shifts absorption toward longer wavelengths and is further influenced by increased crystallinity and doping, achieved through increased film thickness or by applying the plasma treatment before their depositions.[3–7] Overall, more crystallized nc-Si:H layers exhibit reduced short-wavelength absorption and enhanced long-wavelength absorption.

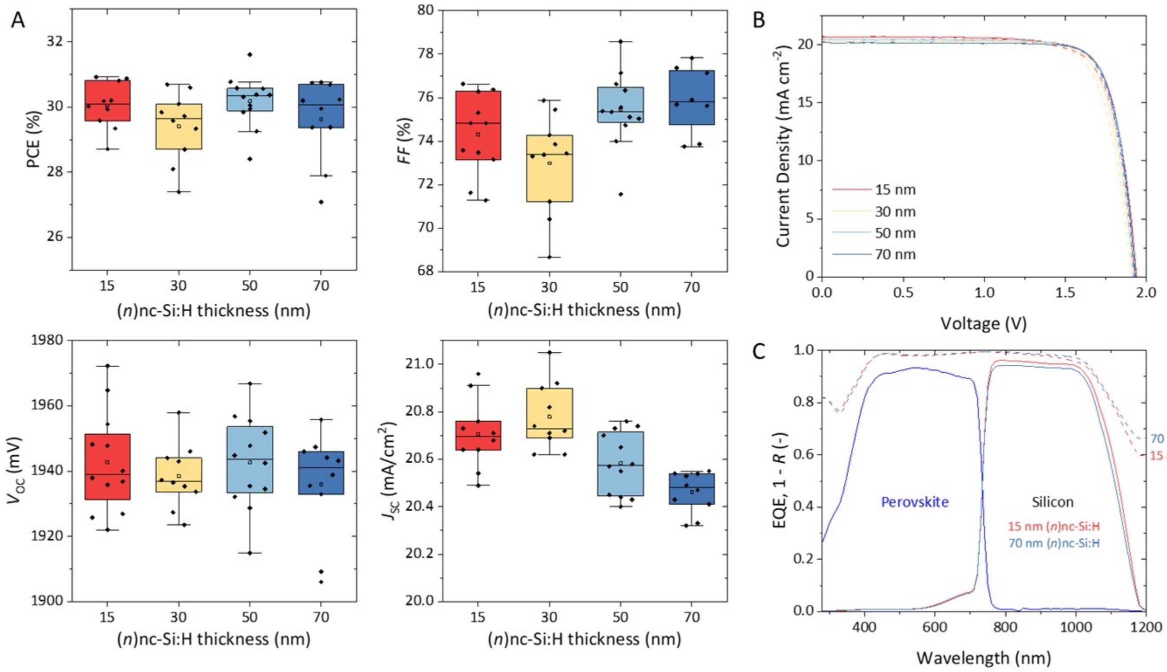

Figure S6. A The *J*-*V* parameters of tandem solar cells featuring (*n*)nc-Si:H with varied thicknesses, **B** the *J*-*V* characteristic of the best devices for each (*n*)-layer, and **C** the EQE and 1 - *R* (reflectance) spectra of tandem solar cells featuring 15-nm-thick and 70-nm-thick (*n*)nc-Si:H layers.

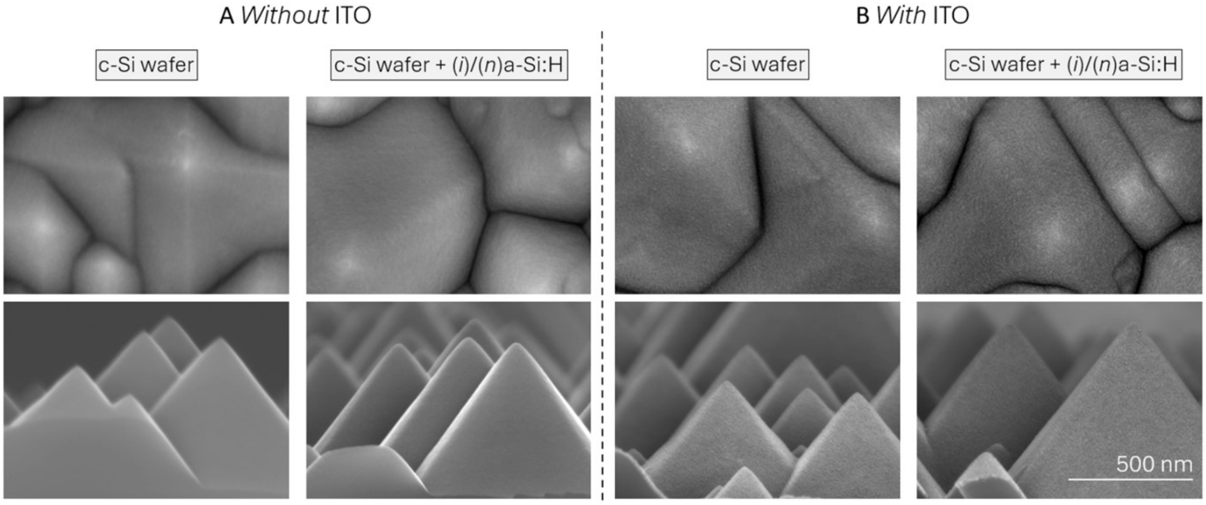

Figure S7. The SEM micrographs of textured c-Si wafers and c-Si samples with (*i*)/(*n*)a-Si:H (6 nm/6 nm) layer stack **A** without and **B** with 10-nm-thick ITO. The top and bottom rows display the top and cross-sectional views, respectively.

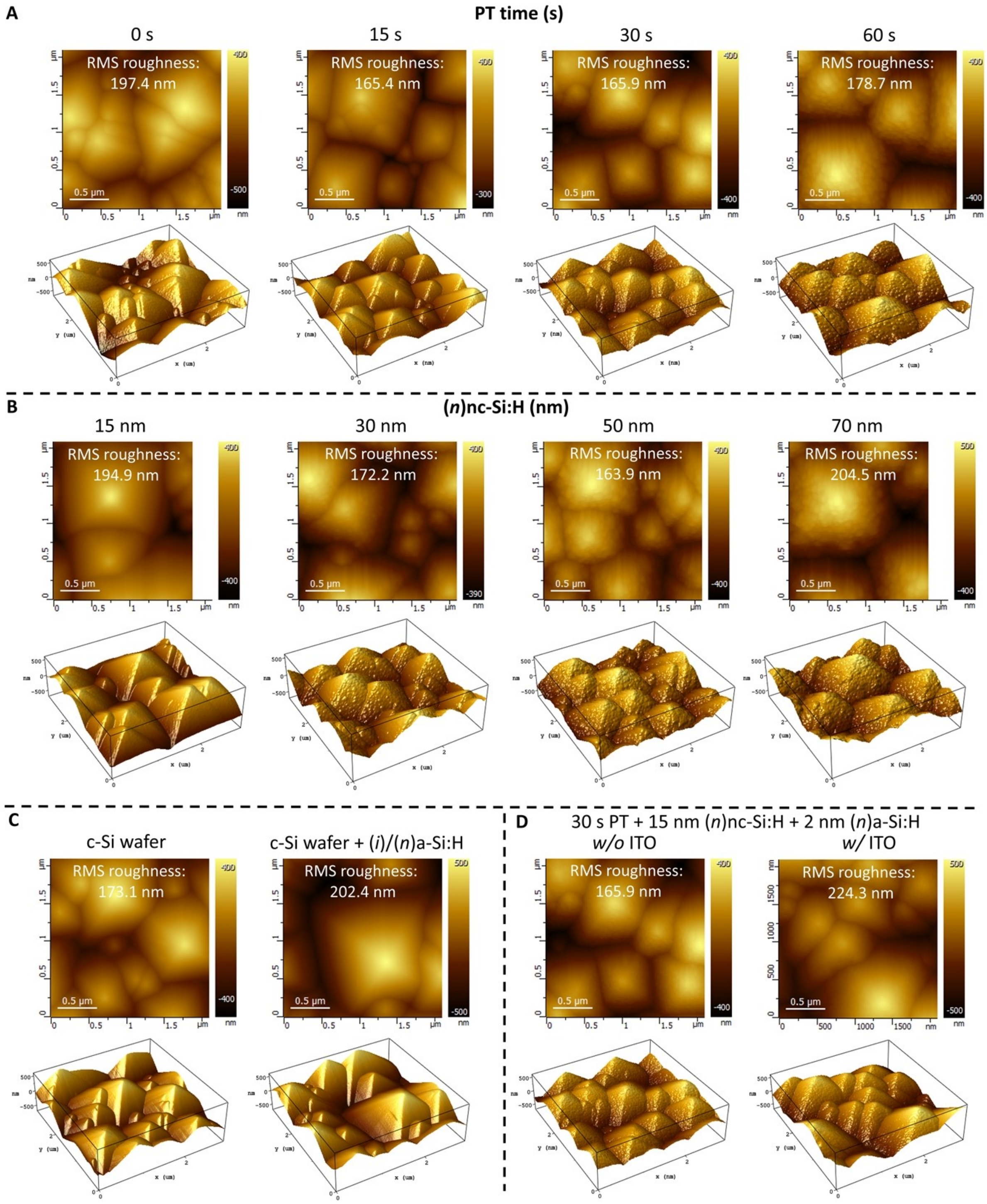

Figure S8. The AFM images (top and bottom rows displaying 2D and 3D images, respectively) of textured c-Si samples with different layer stacks: **A** 15-nm-thick (*n*)nc-Si:H + 2-nm-thick (*n*)a-Si:H layers with different durations of plasma treatment (PT) applied prior to the deposition of (*n*)nc-Si:H layers; **B** varied thicknesses of (*n*)nc-Si:H layers without plasma treatment applied before their depositions; **C** bare c-Si wafer and c-Si wafer with (*i*)/(*n*)a-Si:H layers and **D** 15-nm-thick (*n*)nc-Si:H + 2-nm-thick (*n*)a-Si:H layers, with 30-second-long PT applied before deposition of the (*n*)nc-Si:H layers, without and with a 10-nm-thick ITO layer. Note all samples in figures A, B and D feature 6-nm-thick (*i*)a-Si:H layers underneath the (*n*)-layers (stacks). It is worth noting that roughness quantification and accurate nanoscale information were limited by the dominant pyramidal texture of c-Si wafers, cantilever-facet angle mismatches, and measurement artefacts that prevented reliable capture of fine surface features. Although flat substrates would allow more accurate AFM quantification, they would not fully reflect real device-relevant surfaces. Future work will explore the use of high-aspect-ratio cantilevers, together with leveraging the pyramid facets as reference planes, to enable reliable RMS nanoroughness quantification of layers (stacks) deposited on textured c-Si wafers.

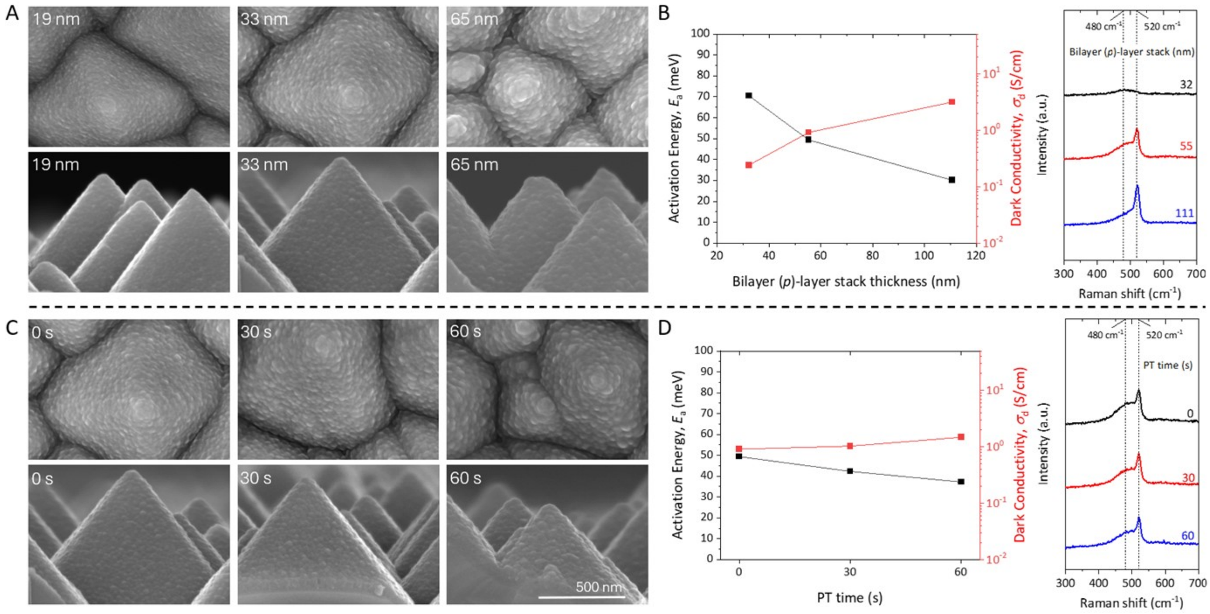

Figure S9. The SEM micrographs of (*i*)a-Si:H-coated (6-nm-thick) textured c-Si samples with **A** varied thicknesses of bilayer (*p*)-layer stacks (5-nm-thick (*p*)nc-SiO_x:H layers together with changing thicknesses of (*p*)nc-Si:H layers) without plasma treatment and **C** different durations of plasma treatment on ~33 nm (*p*)-layer stacks. The top and bottom rows display top views and cross-sectional views, respectively. **B**, **D** The measured activation energy (E_a), dark conductivity (σ_d) and Raman spectra of (*p*)-layer stack with varied conditions are also presented. The (*p*)-layer stack thickness for the PT series to extract E_a and σ_d is around 55 nm. The deposition conditions and material properties of the bilayer (*p*)-layer stacks are reported in a previous publication.[8]

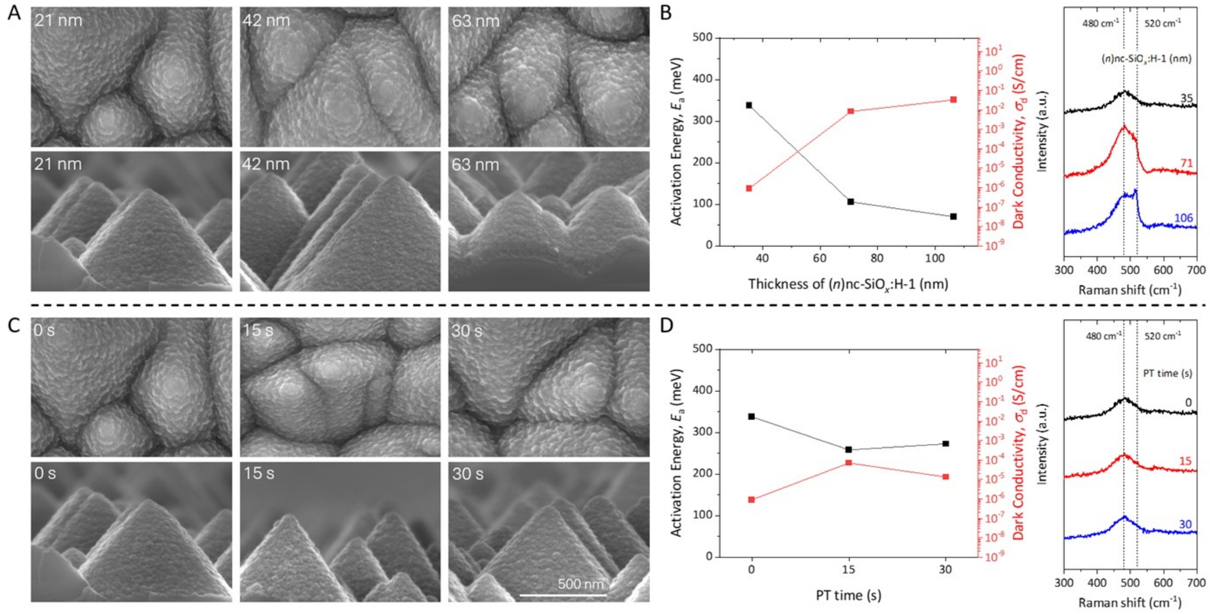

Figure S10. The SEM micrographs of (*i*)a-Si:H-coated (6-nm-thick) textured c-Si samples with **A** varied thicknesses of (*n*)nc-SiO$_x$:H-1 layers without plasma treatment and **C** different durations of plasma treatment on ~21-nm-thick (*n*)nc-SiO$_x$:H-1 layers. The top and bottom rows display top views and cross-sectional views, respectively. **B**, **D** The measured activation energy (E_a), dark conductivity (σ_d) and Raman spectra of (*n*)nc-SiO$_x$:H-1 layers with varied conditions are also presented. The (*n*)nc-SiO$_x$:H-1 layer thickness for the PT series to extract E_a and σ_d is around 35 nm. The deposition conditions and material properties of the (*n*)nc-SiO$_x$:H-1 are reported in a previous publication.[9]

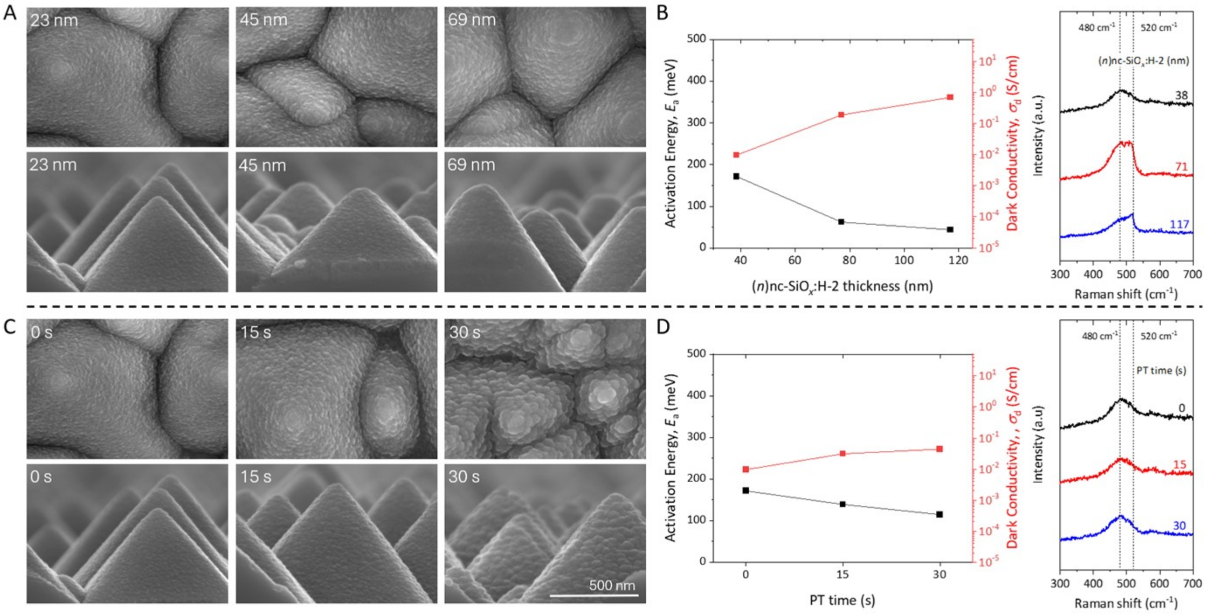

Figure S11. The SEM micrographs of (*i*)a-Si:H-coated (6-nm-thick) textured c-Si samples with **A** varied thicknesses of (*n*)nc-SiO_x:H-2 layers without plasma treatment and **C** different durations of PT on ~23-nm-thick (*n*)nc-SiO_x:H-2 layers. The top and bottom rows display top views and cross-sectional views, respectively. **B**, **D** The measured activation energy (E_a), dark conductivity (σ_d) and Raman spectra of (*n*)nc-SiO_x:H-2 layers with varied conditions are also presented. The (*n*)nc-SiO_x:H-2 layer thickness for the PT series to extract E_a and σ_d is around 38 nm. The deposition conditions and material properties of the (*n*)nc-SiO_x:H-2 are reported in a previous publication.[9]

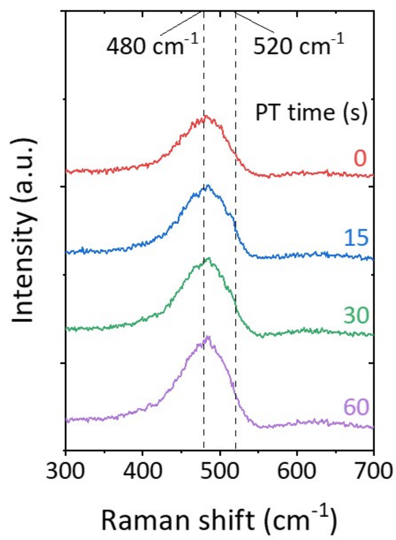

Figure S12. Raman spectra of 15-nm-thick (*n*)nc-Si:H layers with varied durations of the plasma treatment. As the green laser (λ_{laser} = 514 nm) was used, the spectra are dominated by the underlying (*i*)a-Si:H layers, showing insignificant differences with different durations of plasma treatment.

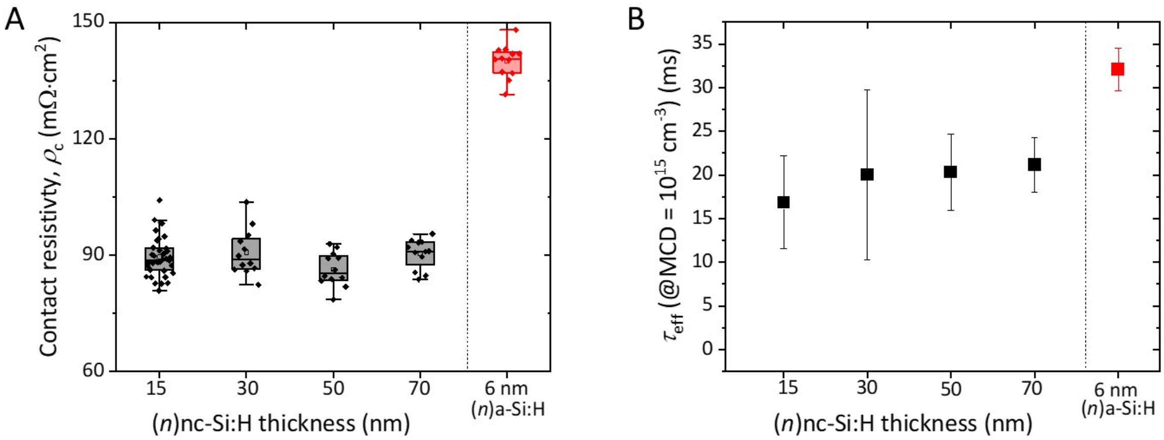

Figure S13. A The contact resistivity (ρ_c) and **B** the effective minority carrier lifetime (τ_{eff}) of symmetric *n*-*n* device stacks as sketched in Figure 2(D) without the plasma treatment. In both figures, the ρ_c and τ_{eff} of samples with 6-nm-thick (*n*)a-Si:H are added for comparison.

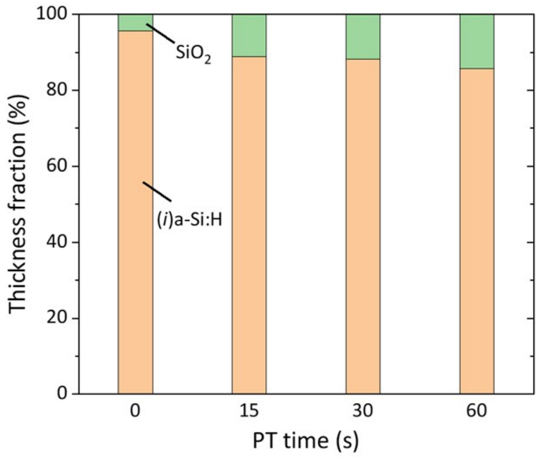

Figure S14. The thickness fractions of (*i*)a-Si:H and SiO_2 in around 13-nm-thick (*i*)a-Si:H layers upon varying plasma treatment (PT) durations. The thickness of each layer was determined via spectroscopic ellipsometry measurements.

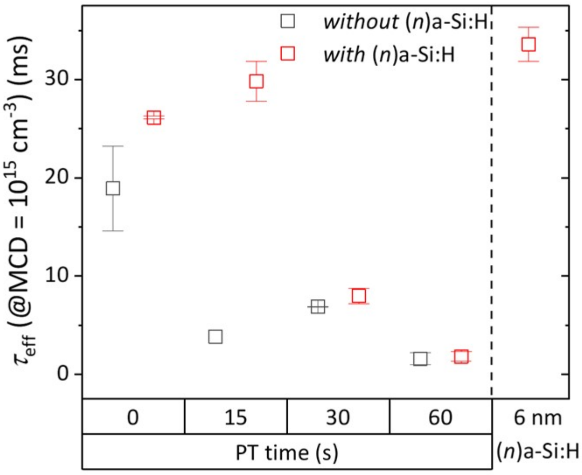

Figure S15. The effective minority carrier lifetime (τ_{eff}) values of symmetrical *n*-*n* samples featuring 15-nm-thick (*n*)nc-Si:H layers, without or with a 2-nm-thick (*n*)a-Si:H capping layer, as a function of plasma treatment duration, before ITO sputtering.

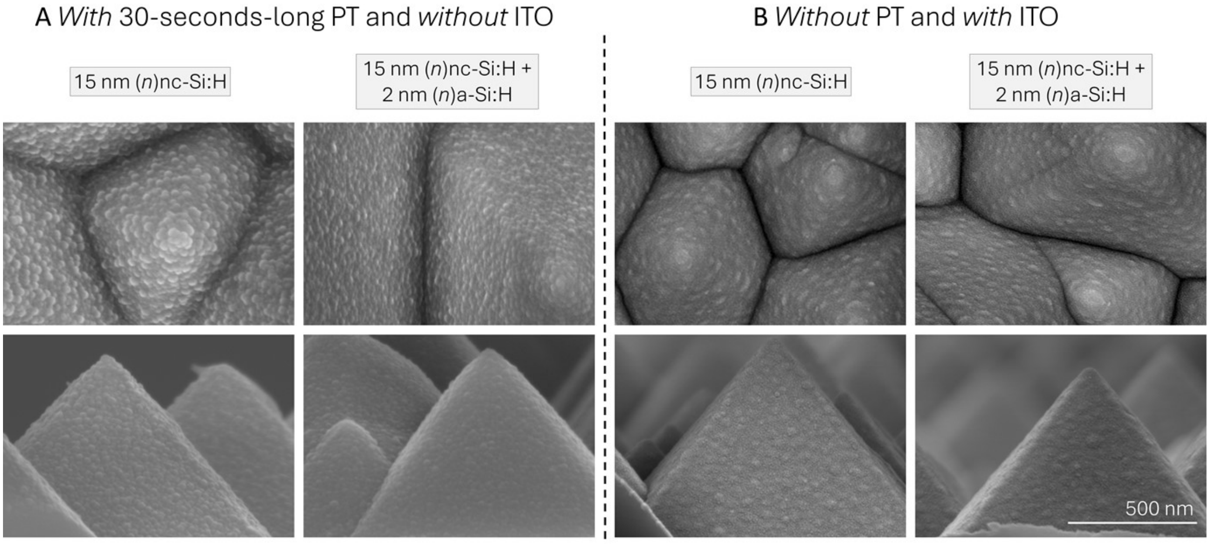

Figure S16. The SEM micrographs of (*i*)a-Si:H-coated (6-nm-thick) textured c-Si samples featuring 15-nm-thick (*n*)nc-Si:H layer and 15-nm-thick (*n*)nc-Si:H + 2-nm-thick (*n*)a-Si:H layer stack **A** with a 30-second-long plasma treatment (PT) prior to (*n*)nc-Si:H deposition and without ITO, and **B** without PT and with 10-nm-thick ITO layers. The top and bottom rows display the top and cross-sectional views, respectively.

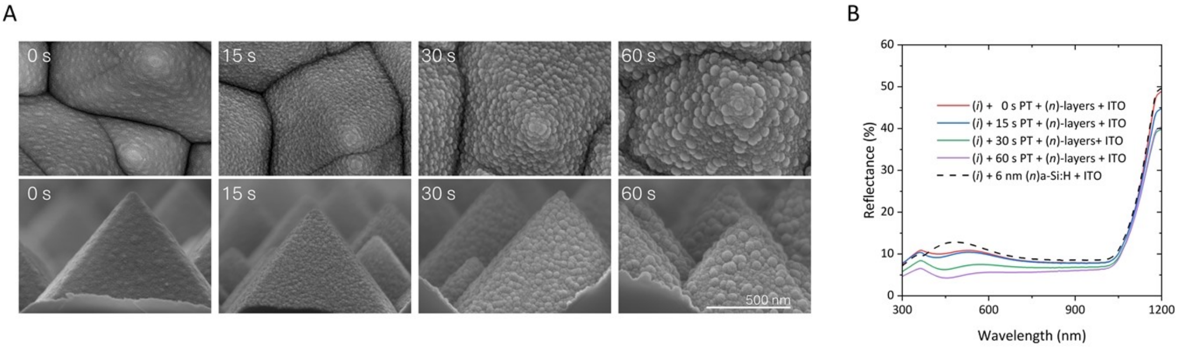

Figure S17. **A** The SEM micrographs (with top and bottom rows displaying top views and cross-sectional views, respectively) and **B** the reflectance spectra of (*i*)a-Si:H-coated (6-nm-thick) textured c-Si samples with 15-nm-thick (*n*)nc-Si:H + 2-nm-thick (*n*)a-Si:H layers ((*n*)-layers) and 10-nm-thick ITO layers with varied durations of PT.

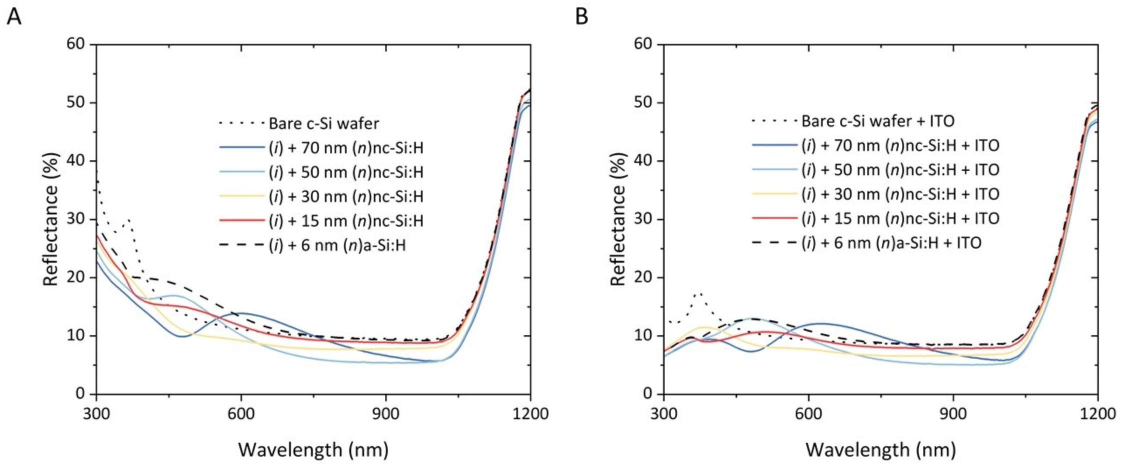

Figure S18. The reflectance spectra of samples featuring varied thicknesses of (*n*)nc-Si:H layers **A** without and **B** with 10-nm-thick ITO layers, on (*i*)a-Si:H-coated (6-nm-thick) textured c-Si substrates. The reflectance spectra of the bare textured c-Si wafer and the sample with 6-nm-thick (*n*)a-Si:H layer are plotted as references.

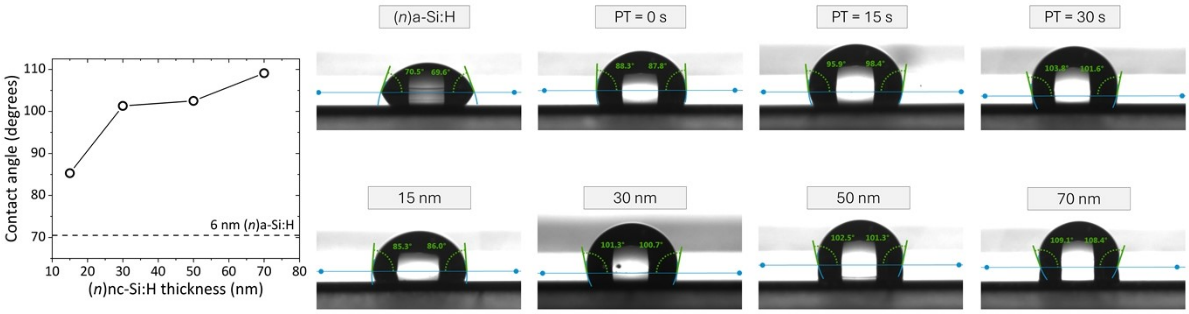

Figure S19. Contact angles after HTL-SAM deposition on textured c-Si wafers featuring various (*n*)-layers with 10-nm-thick ITO. The dashed line in the plot represents the contact angle of the sample with 6-nm-thick (*n*)a-Si:H and 10-nm-thick ITO layers.

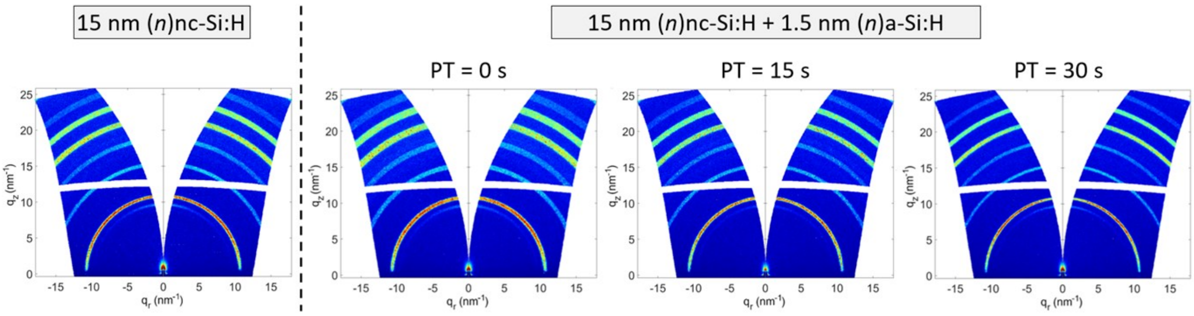

Figure S20. Transformed GIWAXS images of perovskites deposited on samples with various (*n*)-layers.

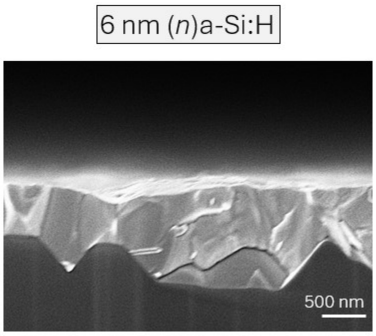

Figure S21. The cross-sectional SEM micrograph of the sample featuring a 6-nm-thick (*n*)a-Si:H layer.

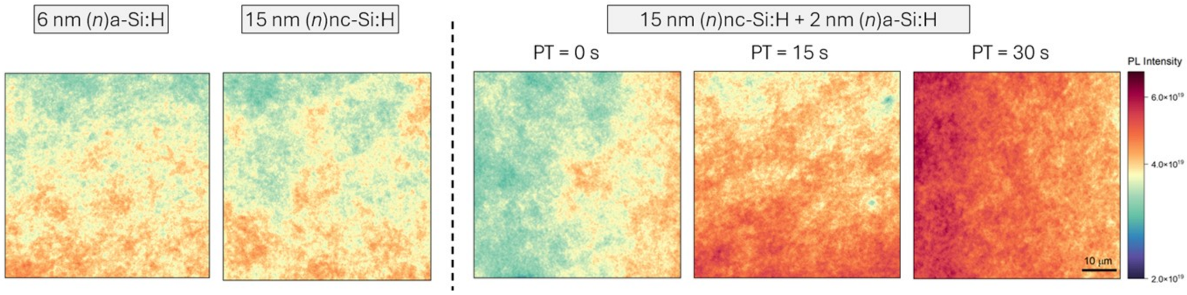

Figure S22. Absolute PL intensity images of perovskites deposited on samples with various (*n*)-layers.

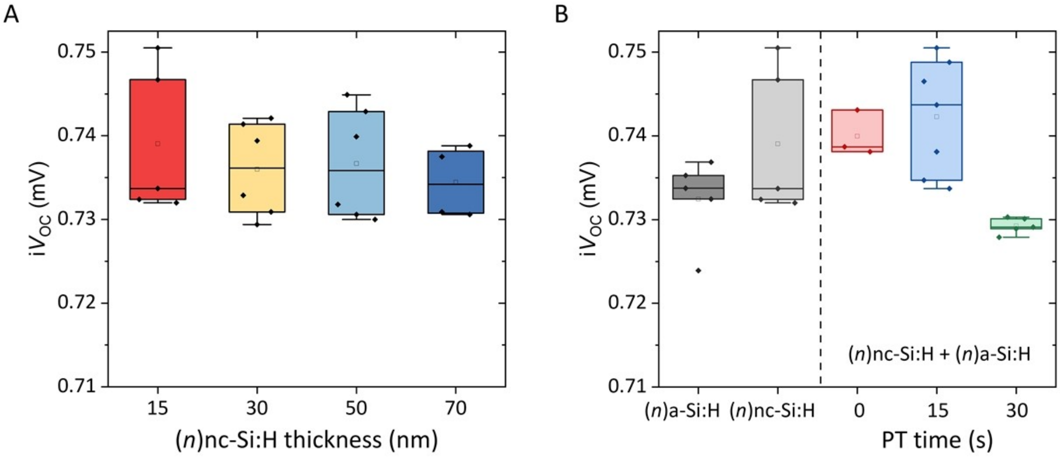

Figure S23. The implied V_{OC} (iV_{OC}) of SHJ bottom-cell precursors corresponding to the structure of (*n*)-layer (stack)/(*i*)a-Si:H/(*n*)c-Si/(*i*)a-Si:H/(*p*)-layer stack, where (*n*)-layer (stack) refers to **A** varied thicknesses of (*n*)nc-Si:H layers without plasma treatment, and **B** various (*n*)-layers (stacks), namely, 6-nm-thick (*n*)a-Si:H layer, 15-nm-thick (*n*)nc-Si:H layer without plasma treatment (labeled as (*n*)nc-Si:H), and 15-nm-thick (*n*)nc-Si:H + 2-nm-thick (*n*)a-Si:H layer stack with varied durations of plasma treatment.

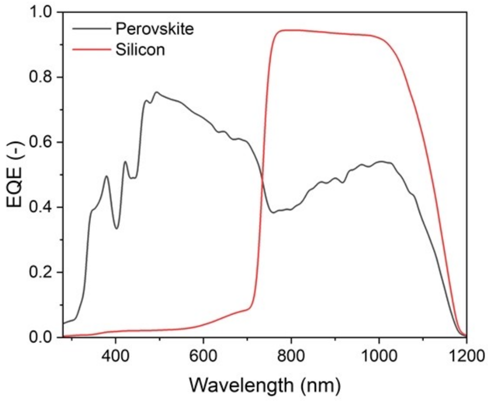

Figure S24. The EQE response of the perovskite-silicon tandem cell based on the silicon bottom cell with a 6-nm-thick (*n*)a-Si:H layer. Note that the long-wavelength response of perovskite top cell can occur when the limiting sub-cell is shunted.

References

1. Li, Q. *et al.* Defects evolution and their impacts on conductivity of indium tin oxide thin films upon thermal treatment. *J Appl Phys* 118, (2015).
2. Aydin, E. *et al.* Enhanced optoelectronic coupling for perovskite/silicon tandem solar cells. *Nature* 623, 732–738 (2023).
3. Usui, S. & Kikuchi, M. Properties of heavily doped GD□ Si with low resistivity. *J Non Cryst Solids* 34, 1–11 (1979).
4. Lubberts, G., Burkey, B. C., Moser, F. & Trabka, E. A. Optical properties of phosphorus-doped polycrystalline silicon layers. *J Appl Phys* 52, 6870–6878 (1981).
5. Köhler, M. *et al.* A silicon carbide-based highly transparent passivating contact for crystalline silicon solar cells approaching efficiencies of 24%. *Nat Energy* 6, 529–537 (2021).
6. Larbi, F. *et al.* Density of states in intrinsic and n/p-doped hydrogenated amorphous and microcrystalline silicon. *Journal of Modern Physics* 2, 1030–1036 (2011).
7. Jackson, W. B. & Amer, N. M. Direct measurement of gap-state absorption in hydrogenated amorphous silicon by photothermal deflection spectroscopy. *Phys Rev B* 25, 5559 (1982).
8. Zhao, Y. *et al.* Design and optimization of hole collectors based on nc-SiOx: H for high-efficiency silicon heterojunction solar cells. *Solar Energy Materials and Solar Cells* 219, 110779 (2021).
9. Zhao, Y. *et al.* Ultra-thin electron collectors based on nc-Si: H for high-efficiency silicon heterojunction solar cells. *Progress in Photovoltaics: research and applications* 30, 809–822 (2022).